Applied Catalysis B: Environmental 246 (2019) 30–40

Contents lists available at ScienceDirect

Applied Catalysis B: Environmental

journal homepage: www.elsevier.com/locate/apcatb

Perovskite oxides for redox oxidative cracking of *n*-hexane under a cyclic redox scheme

Ryan B. Dudek[a], Xin Tian[a,b], Millicent Blivin[a], Luke M. Neal[a], Haibo Zhao[b], Fanxing Li[a,*]

[a] Department of Chemical & Biomolecular Engineering, North Carolina State University, Raleigh, NC, 27695, United States
[b] State Key Laboratory of Coal Combustion, School of Energy and Power Engineering, Huazhong University of Science and Technology, Wuhan 430074, PR China

ARTICLE INFO

Keywords:
Oxidative cracking
Naphtha
Chemical looping
Redox catalyst
Perovskite

ABSTRACT

Steam cracking of naphtha is a commercially proven technology for light olefin production and the primary source of ethylene in the Europe and Asia-Pacific markets. However, its significant energy consumption and high CO_2 intensity (up to 2 tons CO_2/ton C_2H_4), stemming from endothermic cracking reactions and complex product separations, make this state-of-the-art process increasingly undesirable from an environmental standpoint. We propose a redox oxidative cracking (ROC) approach as an alternative pathway for naphtha conversion. Enabled by perovskite oxide-based redox catalysts, the ROC process converts naphtha (represented by *n*-hexane) in an auto-thermal, cyclic redox mode. The addition of 20 wt.% Na_2WO_4 to $SrMnO_3$ and $CaMnO_3$ created highly selective redox catalysts capable of achieving enhanced olefin yields from *n*-hexane oxy-cracking. This was largely attributed to the redox catalysts' high activity, selectivity, and stability towards selective hydrogen combustion (SHC) under a redox mode. Na_2WO_4/$CaMnO_3$ demonstrated significantly higher olefin yield (55–58%) when compared to that from thermal cracking (34%) at 725 °C and 4500 h^{-1}. CO_x yield as low as 1.7% was achieved along with complete combustion of H_2 over 25 cycles. Similarly, Na_2WO_4/$SrMnO_3$ achieved 41% olefin yield, 0.4% CO_x yield, and 73% H_2 combustion at this condition. Oxygen-temperature-programmed desorption (O_2-TPD) indicated that Na_2WO_4 hindered gaseous oxygen release from $CaMnO_3$. Low-energy ion scattering (LEIS) and X-ray photoelectron spectroscopy (XPS) revealed an outermost perovskite surface layer covered by Na_2WO_4, which suppressed near-surface Mn and alkaline earth metal cations. The formation of non-selective surface oxygen species was also inhibited. XPS analysis further confirmed that promotion of $SrMnO_3$ with Na_2WO_4 suppressed surface Sr species by 90%, with a similar effect also observed on $CaMnO_3$. These findings point to the promoting effect of Na_2WO_4 and the potential of promoted $SrMnO_3$ and $CaMnO_3$ as selective redox catalysts for efficient production of light olefins from naphtha via the ROC process.

1. Introduction

Ethylene is a critical building block in the chemical industry, with a worldwide market totaling 148 million tonnes in 2014 [1,2]. Steam cracking of hydrocarbon feedstocks (ethane, naphtha, *etc.*) is the leading technology for ethylene production, but it is also one of the most energy- and CO_2-intensive processes in the chemical industry; in 2010, 1.9 exajoules of energy were consumed and 120 Mt CO_2-eq emitted solely as a result of ethylene production via steam cracking [3,4]. With the global ethylene market projected to grow by as much as 400% by 2050, new process technologies are needed to maintain this growth while reducing the environmental impacts of ethylene production [5].

In Europe and the Asia-Pacific region, steam cracking of full-range naphtha (boiling point range of 35–180 °C) is the primary source of ethylene production; worldwide, naphtha constitutes 55% of all steam cracking feedstocks [1,3]. In a typical naphtha steam cracking process, naphtha is vaporized and pre-heated in the convective zone of the furnace and mixed with diluting steam (0.4–0.5 kg/kg feed) before entering the radiant tube (750–900 °C) and cracking into smaller molecules via free-radical reactions [1,3,6]. A subsequent quenching step preserves the light olefins formed. Steam cracking requires significant heat for steam generation, naphtha vaporization, and the endothermic cracking reactions. This heat requirement is met by combusting carbonaceous fuels such as fuel oil and/or natural gas, resulting in significant energy usage and up to 2 ton CO_2 / ton ethylene produced [3,7]. Aside from heat supplied for cracking, the wide range of gaseous products generated through steam cracking necessitates an extensive

* Corresponding author.
E-mail address: fli5@ncsu.edu (F. Li).

https://doi.org/10.1016/j.apcatb.2019.01.048
Received 1 November 2018; Received in revised form 8 January 2019; Accepted 16 January 2019
Available online 17 January 2019
0926-3373/

separation train which consumes additional energy. Novel approaches that can reduce the energy- and CO_2-intensity for light olefin production from naphtha are highly desirable.

While catalytic cracking in the presence of heterogeneous catalysts (*e.g.* zeolites) can decrease the temperature of the cracking reactions, the heat requirements associated with naphtha vaporization and pyrolysis are still present [8,9]. To balance these heat requirements, multiple process alternatives have been proposed in recent years. Liu et al. proposed a gas phase oxidative cracking process which gave 50% yield of light alkenes from *n*-hexane (as a model compound for naphtha) in the presence of gaseous oxygen at 750 °C, but combustion reactions led to 12–13% CO_x yield [10,11]. Boyadjian et al. used Li/MgO catalysts in combination with gaseous O_2 in a catalytic oxidative cracking process to achieve 17% light olefin yield from *n*-hexane at 575 °C; the corresponding CO_x yield was 7% [12]. In a subsequent process analysis, feedstock loss to CO_x was shown to significantly harm the process economics [13]. In both studies, co-feeding of gaseous oxygen with hydrocarbons introduces an inherent flammability hazard and reduces olefin yields. Oxygen production via cryogenic air separation is also energy- and capital-intensive.

Chemical looping provides a strategy for separating oxidative processes into two-step, cyclic redox processes in spatially separate reactors to mitigate the challenges related to oxygen co-feed [14,15]. In this study, we demonstrate a redox oxidative cracking (ROC) concept for naphtha conversion in absence of O_2 [7]. In the ROC process, as illustrated in Fig. 1, vaporized naphtha is cracked at temperatures above 500 °C to form light olefins and hydrogen [7,16]. The resulting hydrogen is selectively combusted by the lattice oxygen of a metal oxide redox catalyst to form water [7]. The reduced redox catalyst is then re-oxidized with air in a separate regeneration reactor, completing the redox cycle. In a study by Elbadawi et al., lattice oxygen from VO_x/Ce-Al_2O_3 was used to drive a combined n-hexane cracking and oxidative dehydrogenation (ODH) reaction between 525 °C and 600 °C in an oxidative cracker, with a separate regenerator reactor restoring the lattice oxygen. While this redox catalyst showed stable behavior over many redox cycles at 550 °C, the olefin selectivity (60%) and hexane conversion (30%) were relatively limited [16]. In contrast, we recently showed that ROC of naphtha with a manganese-containing redox catalyst has the potential to reduce thermal energy demand by 52% and CO_2 emissions by over 50% in comparison to steam cracking while slightly improving light olefin yields [7,17]. Given the importance of redox catalysts to the overall performance of ROC, further development and optimization of redox catalysts is highly desirable.

Our recent studies on chemical looping-oxidative dehydrogenation (CL-ODH) of ethane indicate that manganese-based redox catalysts capable of selective hydrogen combustion (SHC) can enhance olefin yields from ethane cracking by 25% at 850 °C [18,19]. In addition to increasing yields, combustion of the hydrogen co-product in CL-ODH enabled auto-thermal operation of the ethane cracking reactor [20]. While a similar strategy can be applied for naphtha cracking, lower operating temperatures are required than those for ethane cracking. Recently, we identified a promising set of Mn-containing perovskite oxides capable of performing SHC in the presence of ethylene across a wide range of temperatures. With demonstrably high selectivity and activity values in the range from 650 °C to 800 °C, $SrMnO_3$- and $CaMnO_3$-based redox catalysts are potentially suitable for the ROC of naphtha [21].

In this work, we investigated the merits of perovskite oxides applied in the redox oxidative cracking of *n*-hexane as a model compound for naphtha. Strontium manganate ($SrMnO_3$) and calcium manganate ($CaMnO_3$) were synthesized both in as-prepared forms and with sodium tungstate promotion (20 wt.% Na_2WO_4). The performance of these redox catalysts was explored across a range of temperatures and gas flowrates. Na_2WO_4-promoted $SrMnO_3$ and $CaMnO_3$ were capable of achieving olefin yields in excess of the thermal background (*e.g.* 57% vs. 41% olefin yield at 750 °C) while maintaining low CO_x yields (4% at 750 °C) and combusting most of the H_2 produced during cracking (83%). Characterization including O_2-TPD, XPS, LEIS, and XRD were used to study interactions between each perovskite oxide and the Na_2WO_4 dopant and correlate the structure and near-surface composition with reaction performance. Furthermore, $Na_2WO_4/SrMnO_3$ and $Na_2WO_4/CaMnO_3$ were evaluated in terms of their cycling stability and long-term performance for ROC of *n*-hexane under a cyclic redox scheme.

2. Experimental

2.1. Synthesis of redox catalysts

$SrMnO_3$ (strontium manganate) and $CaMnO_3$ (calcium manganate) were prepared via a modified Pechini method described elsewhere [21]. Briefly, stoichiometric amounts of $Mn(NO_3)_2{\cdot}4H_2O$ (97.0%, Sigma-Aldrich) and either $Sr(NO_3)_2$ (99.0%, Noah) or $Ca(NO_3)_2{\cdot}4H_2O$ (99.0%, Sigma-Aldrich) were dissolved in deionized water and stirred at 40 °C. Citric acid (99.5%, Sigma-Aldrich) was then added into the solution at a molar ratio of 2.5:1 to metal ions (Mn^{2+} and either Sr^{2+} or Ca^{2+}). The solution was kept stirring at 500 rpm and 40 °C for 30 min. Afterwards, ethylene glycol (99.8%, Sigma-Aldrich) in a molar ratio of 1.5:1 to citric acid was introduced to the mixture to promote gel formation. The solution was heated to 80 °C with continuous stirring until a viscous gel formed, then dried overnight at 100 °C in an oven. The dried precursor was first pre-treated in a muffle furnace at 450 °C for 3 h to burn off nitrates, and then calcined in a tube furnace (GSL-15 0X, MTI Corporation) at 1000 °C for 12 h under continuous air flow. The high temperature sintering contributed to the formation of $SrMnO_3$ and $CaMnO_3$ perovskite oxides.

Promotion of the as-obtained $SrMnO_3$ and $CaMnO_3$ materials with 20 wt.% Na_2WO_4 was done by wet impregnation. Calculated amount of $Na_2WO_4{\cdot}2H_2O$ (99.0%, Sigma-Aldrich) was mixed with deionized water and added dropwise to the base perovskite oxides. After being stirred every 15 min until dry, it was kept overnight at 80 °C in an oven. Finally, the promoted samples, namely $Na_2WO_4/SrMnO_3$ and Na_2WO_4/

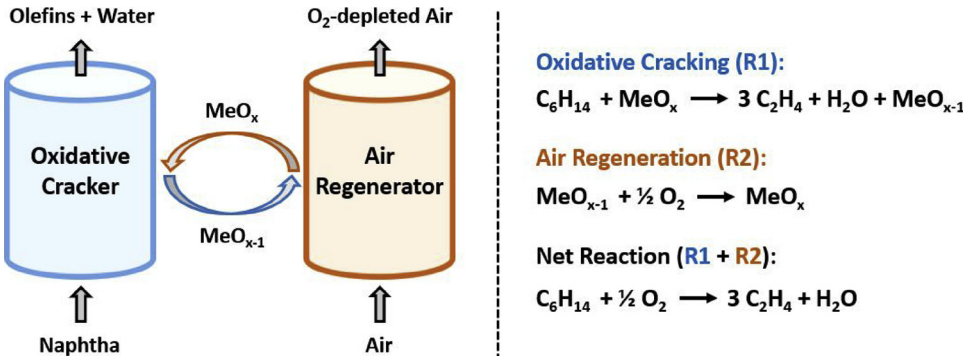

Fig. 1. A block flow diagram for the redox oxidative cracking (ROC) of naphtha concept, using the simplified net reaction $C_6H_{14} \rightarrow 3\ C_2H_4 + H_2$ to represent thermal cracking of naphtha with *n*-hexane as a model compound. MeO_x represents a fully oxidized perovskite-type mixed metal oxide while MeO_{x-1} indicates lattice oxygen has been donated.

$CaMnO_3$, were calcined again at 900 °C for 6 h. All catalysts were ground and sieved into the size range of 250–850 μm for reaction testing. Powders smaller than 250 μm were used for characterization.

2.2. Characterization of redox catalysts

Powder X-ray diffraction (XRD) experiments were conducted to determine the crystal phase of both the as-prepared and cycled redox catalysts, using a Rigaku SmartLab X-ray diffractometer. The radiation source was monochromatic Cu Kα with $\lambda = 0.1542$ nm, operated at 40 kV and 44 mA. A continuous scan method within a 2θ range of 10-80° was adopted to generate XRD patterns, with a step size of 0.05° and holding at each step for 3 s. The crystal phases were determined using the International Center for Diffraction Data (ICDD) database in HighScore Plus software.

X-ray photoelectron spectroscopy (XPS) was adopted for near-surface composition analysis of the fresh and cycled redox catalysts. The XPS system consisted of a Thermo-Fisher Alpha 110 hemispherical energy analyzer, a Thermo-Fisher XR3 and 300 W dual-anode X-ray source, with Al anode (1486.7 eV) as the excitation source. For each catalyst, XPS narrow scans were taken for all metal cations present (Sr 3*d*, Ca 2*p*, Mn 2*p* and 3*s*, Na 1*s*, W 4*f*), along with C 1*s* and O 1*s*. XPS patterns were analyzed by the CasaXPS program (Casa Software Ltd., U.K.). An adventitious C 1*s* peak at 284.6 eV was used for calibration of all binding energies.

Low-energy ion scattering (LEIS) was conducted at the Surface Analysis Center at Lehigh University on an ION-TOF Qtac^{100} spectrometer to obtain surface compositional information. A 3 keV He^+ (2×10^{14} ions cm^{-2}, 1.0 x 1.0 mm raster) primary ion beam was used at 3000 eV pass energy, while a 0.5 keV Ar^+ sputtering source (0.5 or 1.0×10^{15} cm^{-2} cyc^{-1}, 2.0 x 2.0 mm or 1.5 x 1.5 mm raster) was used at 30° angle to the sample surface for depth profiling; during spectra acquisition and sputtering, charge neutralization was invoked. Prior to analysis, sample powders were dispersed into a sample holder and compressed by 2000 psi.

To investigate the reducibility of the catalysts as well as the onset temperature of reaction, *n*-hexane temperature-programmed reaction (TPR) experiments of the four as-prepared catalysts were carried out using a 1/8 in. ID fixed-bed quartz U-tube reactor. Heat was provided to the reactor externally by a tube furnace equipped with a K-type thermocouple. In each run, 0.5 g of catalyst (250–850 μm) was loaded into the reactor. For comparison, a blank *n*-hexane TPR with inert Al_2O_3 (16 mesh) was also conducted. Prior to TPR tests, the samples were first pre-treated at 900 °C in 10 vol.% O_2 (balance Ar, with a total flowrate of 100 mL/min) for 30 min to fully oxidize and clean the surface of the catalyst. After cooling down to room temperature, the catalyst samples were then heated from 450 °C to 750 °C at 5 °C/min under ~13 vol.% *n*-hexane flow. 75 mL/min Ar carrier gas (a relatively low flowrate as compared to later tests) was used in order to amplify product signals on the mass spectrometer. Gas products generated in the reaction were analyzed by an MKS Cirrus II mass spectrometer, and volumetric flowrates of several primary gases (H_2, C_2H_4, CO_2, C_6H_{14}) were calculated using three-point calibrations (m/z = 2, 26, 44, and 57, respectively; m/z = 26 from ethylene was deconvoluted from ethane and *n*-hexane).

Oxygen and carbon dioxide temperature-programmed desorption experiments (O_2-TPD and CO_2-TPD) were performed on a SETARAM Setsys Evolution Thermal Gravimetric Analyzer (TGA-DTA/DSC) using redox catalyst samples in the particle size range 150–250 μm. In a typical O_2-TPD experiment, 40–60 mg of catalyst was cycled three times between 10% H_2 / 10% O_2 using a carrier gas flow of 180 mL/min He at 750 °C. The sample was then maintained under 10% O_2, ramped to 900 °C at 20 °C/min, held at 900 °C for 30 min, and cooled to 150 °C at 10 °C/min. After purging for 1 h in He, the sample was ramped to 900 °C at 5 °C/min and mass loss was recorded. For CO_2-TPD experiments, 40–50 mg redox catalyst was heated to 900 °C at 20 °C/min under 10% CO_2 (with 180 mL/min He) and held there for 30 min, then cooled to 150 °C at 10 °C/min. The sample was then purged in He for 1 h and ramped to 900 °C at 5 °C/min.

2.3. n-hexane oxidative cracking test conditions

Oxidative cracking experiments with *n*-hexane were conducted in a 1/8 in. ID fixed-bed quartz U-tube reactor heated externally by a furnace controlled with a K-type thermocouple. Cycling between reduction and oxidation steps were achieved using an automated valve switching system. Each experiment used 0.5 g (approximately 1 mL volume) of redox catalyst sized 250–850 μm, with 16 mesh Al_2O_3 grit loaded into the remaining void space on either side of the fixed bed to limit the gas volume in the heated zone. For quantification of thermal background conversion and yields, the redox catalyst was replaced with Al_2O_3 grit at the same testing conditions.

Prior to *n*-hexane oxy-cracking tests, samples were pre-treated at 750 °C with five redox cycles comprising a 3 min reduction step of 80 vol.% ethane/Ar (total flowrate of 75 mL/min) and a 3 min oxidation step of 17 vol.% O_2/Ar (total flowrate of 90 mL/min) to achieve stabilized redox characteristics. During a typical n-hexane cracking experiment, up to 6 different temperature conditions (650–775 °C, 25 °C increments) were evaluated at a constant gas hourly space velocity, GHSV = 9000 h^{-1}. A lowered GHSV = 4500 h^{-1} was also used during redox catalyst stability experiments to achieve deeper reduction and greater redox stress, conditions which are more likely to expose stability or coke resistance issues. Vapor-phase *n*-hexane was introduced into the reactor by flowing the inlet Ar stream into a stainless steel bubbler containing liquid *n*-hexane maintained at 20 °C. Condensation of liquid *n*-hexane was avoided throughout the procedure by saturating the Ar stream at several degrees below room temperature and by diluting the saturated stream ($y_{hexane} = 0.159$) with pure Ar in a 4:1 ratio prior to the reactor, resulting in a final *n*-hexane concentration of $y_{hexane} = 0.127$, below the saturation limit at 23 °C. In a typical test at GHSV = 9000 h^{-1}, 120 mL/min Ar was introduced into the bubbler to generate saturated *n*-hexane/Ar flow and another 30 mL/min Ar was added before entering the U-tube reactor for 20 s reaction duration. During the oxidation step, 150 mL/min Ar + 30 mL/min O_2 (resulting in 16.7 vol.% O_2) was used to regenerate the reduced catalyst for 3 min A five-minute purge step with 150 mL/min Ar was introduced before and after each reduction step. For each condition, four redox cycles were conducted and the effluent gas from the third reduction step was collected in a sample gas bag for gas chromatography. Furthermore, to verify the stable cyclic redox characteristics of the two promoted samples, longer-term experiments with 25 redox cycles were conducted at 4500 h^{-1} GHSV and 725 °C. To ensure a constant volume of *n*-hexane injection at 4500 h^{-1} compared to 9000 h^{-1}, the injection time was doubled.

A gas chromatograph (GC, Agilent Technologies 7890B), with a flame ionization detector (FID) channel for hydrocarbon analysis and two thermal conductivity detector (TCD) channels for H_2 (Ar/TCD channel) and CO_x (He/TCD channel) identification, was used to analyze the outlet gas (collected by a gas sampling bag) during the reduction step. Before measurements, a refinery-grade gas calibration standard was used to calibrate the GC signals. The volume percentage of different gas species was calculated by integrating the signal peak. The conversion of *n*-hexane and selectivity to all carbonaceous products were calculated on a molar carbon basis. H_2O formation was calculated on the basis of atomic H balance of all observed products. The whole product distribution was used to calculate the approximate oxygen donation (in wt.%) by the redox catalyst at each condition via the method given in Supporting Information. All cycles not analyzed via GC were measured by the MKS Cirrus II mass spectrometer and used to quantify coke (i.e. CO_x upon regeneration) as well as to verify GC results.

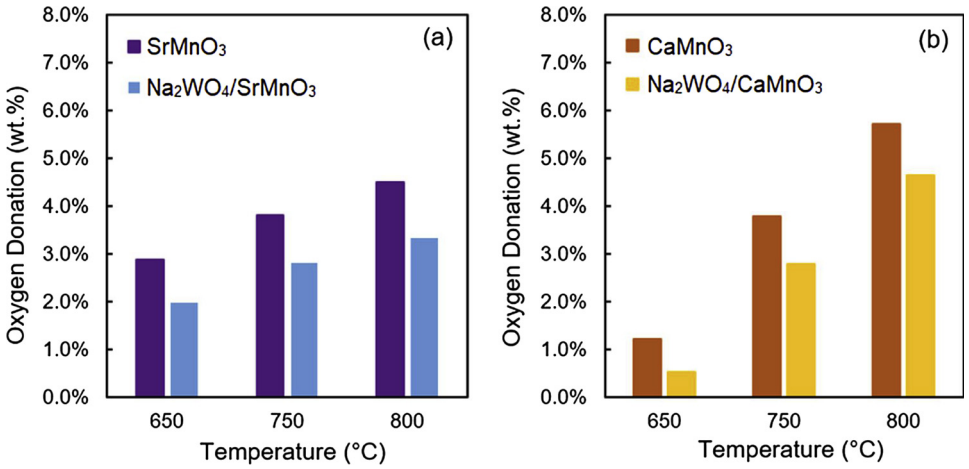

Fig. 2. Oxygen donation by (a) $SrMnO_3$, $Na_2WO_4/SrMnO_3$, and (b) $CaMnO_3$, $Na_2WO_4/CaMnO_3$, as determined by material balance on H_2/C_2H_4 co-feed experiments in a U-tube reactor. Conditions: F = 100 mL/min, $y_{H2}/y_{C2H4}/y_{Ar}$ = 0.4/0.4/0.2, m = 100 mg, step duration = 10 s.

3. Results and discussion

3.1. Perovskites as redox catalysts

Ethylene is the major hydrocarbon species produced from the *n*-hexane cracking reaction, while hydrogen is a byproduct that can be selectively combusted to provide the energy for the endothermic cracking reaction. Our previous work has demonstrated the effectiveness of $SrMnO_3$ and $CaMnO_3$ as oxygen donors capable of selective H_2 combustion (SHC) in the presence of ethylene and hydrogen [21]. Therefore, these redox catalysts are investigated here for ROC applications. Na_2WO_4 was selected as a "promoter" since it was shown to be effective for inhibiting undesired CO_x formation in ODH and SHC reactions [18,19,21,22]. Unlike conventional heterogenous catalysts, an important function of the redox catalyst is to carry and donate its active lattice oxygen in the oxidative cracking reaction. As such, oxygen storage capacities of both the unpromoted and Na_2WO_4-promoted perovskite redox catalysts were determined first.

Fig. 2 shows the oxygen donation achieved by four redox catalysts during 10-second step experiments in the presence of a H_2/C_2H_4 mixture. As can be seen, oxygen carrying capacities of Na_2WO_4-promoted redox catalysts are lower than their unpromoted counterparts. Nevertheless, all four redox catalysts exhibited satisfactory oxygen capacity within the temperature range of interest. It is also noted that the lattice oxygen of redox catalysts employed in partial oxidation processes such as ROC can be utilized more effectively compared to complete combustion processes, *e.g.* chemical looping combustion (CLC). For instance, CLC of *n*-hexane would consume up to 19 times more lattice oxygen than *n*-hexane ROC (see Supporting Information). Therefore, the oxygen capacities demonstrated by the four redox catalysts become potentially more attractive when lattice oxygen utilization in ROC is considered. Specific surface areas of the redox catalysts are summarized in Table S1 (supplementary).

3.2. Olefin yield comparisons

Accurate evaluation of the role of catalysts, including redox catalysts, for ODH and oxy-cracking reactions can be affected by potential contributions from thermal cracking, especially at higher operating temperatures. While redox catalysts can significantly enhance single-pass olefin yield through SHC even if they are largely inactive for C—H bond activation [18,19], catalytic activity for alkane activation is nevertheless desirable for redox catalysts due to the possibility of lowering the operating temperature and/or residence time [23,24]. We employed a combination of temperature-programmed and isothermal experiments to establish that $SrMnO_3$- and $CaMnO_3$-based redox catalysts are capable of generating ethylene yields in excess of the thermal background in an *n*-hexane cracking setting. Temperature-programmed reaction (TPR) experiments were first conducted to assess the activity and reducibility of four redox catalysts under *n*-hexane flow in comparison to a thermal background TPR over inert alumina grit. The results of the five *n*-hexane TPR experiments are shown in Fig. 3 in the form of ethylene product flow, incremental ethylene flow over the background, and incremental CO_2 product flow over the background.

Fig. 3a–b indicates that each of the four redox catalysts initiates ethylene formation at a lower temperature compared to *n*-hexane thermal cracking. *n*-Hexane reacts on the redox catalysts to produce ethylene at temperatures as low as 600 °C, and the ethylene yield improvement over the background is the most significant around 650 °C; for $CaMnO_3$ vs. thermal background, this difference is 1.2 mL/min C_2H_4 vs. 0.3 mL/min C_2H_4, or 4 C% yield towards C_2H_4 vs. 1 C% C_2H_4 yield. Thermal cracking of *n*-hexane to its products becomes dominant over surface-initiated reactions (*i.e.* over a redox catalyst) at temperatures of 700 °C and above.

Formation of CO_x is important in identifying the selectivity of redox catalysts towards hydrogen combustion (*i.e.* SHC) relative to oxidation of hydrocarbons (*n*-hexane fed, C_2H_4 produced, *etc.*). Loss via non-selective combustion would lead to CO_x formation and hence decrease the selectivity of desired olefin products. Generally, CO yields were insignificant compared to those of CO_2 in both TPR and isothermal experiments. Fig. 3c shows that in the case of the $CaMnO_3$ redox catalyst, lower-temperature activation of *n*-hexane resulted in both C_2H_4 and CO_2 (*e.g.* for $CaMnO_3$ at 650 °C, 0.6 C% CO_2 yield vs. 3.8 C% C_2H_4 yield). Promotion of $CaMnO_3$ with 20 wt.% Na_2WO_4 led to a higher onset temperature for C_2H_4 formation and suppression of CO_2 generation until above 700 °C. Meanwhile, $SrMnO_3$ and $Na_2WO_4/SrMnO_3$ did not yield appreciable amounts of CO_2 at temperatures below 750 °C during the TPR; however, the observed low CO_x selectivity from TPR experiments cannot be directly used to predict the redox catalyst performance at high-temperature isothermal conditions, due to the gradual removal of both selective and non-selective oxygen species at lower temperatures during the TPR [21].

Isothermal *n*-hexane oxy-cracking experiments over $Na_2WO_4/CaMnO_3$ feature olefin yields significantly higher than those from the background thermal cracking between 650 °C and 775 °C (Fig. 4). Comprehensive reaction data for several background thermal cracking conditions are given in Table S2. The improvement in olefin yield by $Na_2WO_4/CaMnO_3$ is most significant at 750 °C, where the yield increases by 35% over the background (55% vs. 41%). The yield increase observed across these conditions is mostly attributed to a

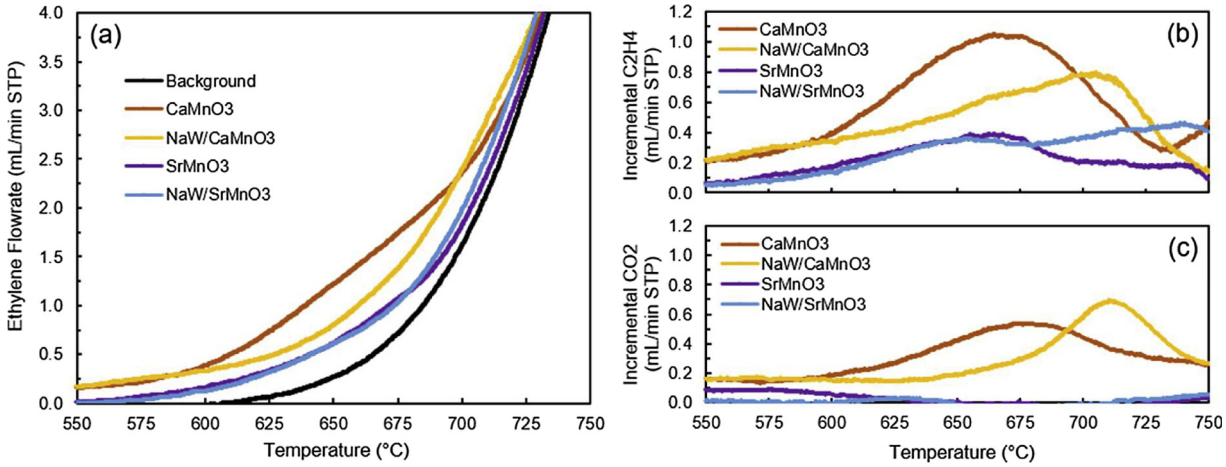

Fig. 3. Results from *n*-hexane TPR on four redox catalysts and accompanying thermal background, showing in STP mL/min (a) ethylene product flowrate, (b) incremental ethylene flowrate over the background, and (c) incremental CO_2 product flowrate over the background CO_2 (equal to zero). Ethylene production above the thermal background indicates *n*-hexane activation by the redox catalyst, while CO_2 production indicates undesired side reactions. Results were obtained via mass spectrometry. Conditions: GHSV = 4500 h^{-1} (F_{Ar} = 75 mL/min, m = 500 mg), $y_{n\text{-hexane}} \approx 0.13$, ramping rate of 5 °C/min.

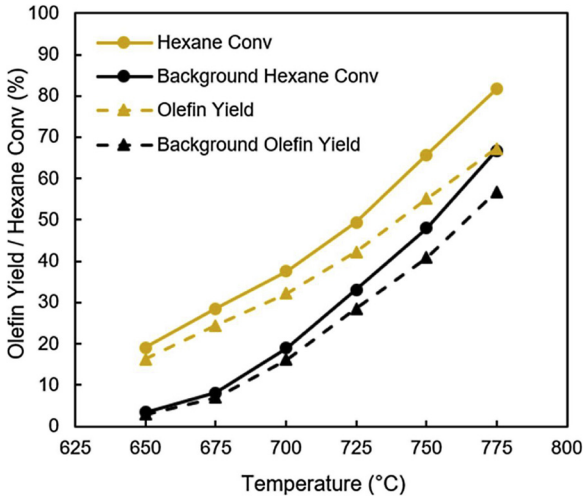

Fig. 4. A comparison of *n*-hexane conversion and olefin yields over the $Na_2WO_4/CaMnO_3$ redox catalyst with those from the thermal cracking background. Conditions: GHSV = 9000 h^{-1} (F_{Ar} = 150 mL/min, m = 500 mg), $y_{n\text{-hexane}} \approx 0.13$, step duration = 20 s.

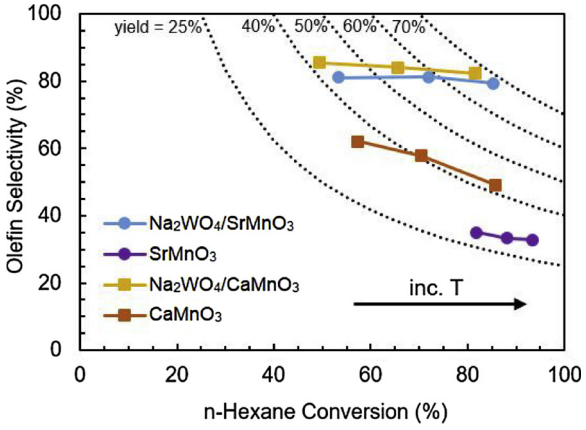

Fig. 5. Olefin yields achieved by four redox catalysts. From left to right: T = 725 °C, 750 °C, 775 °C. Constant yield contours indicate the product of *n*-hexane conversion and olefin selectivity for each data point, with selectivity on a carbon basis. Results obtained via GC. Conditions: GHSV = 9000 h^{-1} (F_{Ar} = 150 mL/min, m = 500 mg), $y_{n\text{-hexane}} \approx 0.13$, step duration = 20 s.

commensurate increase in *n*-hexane conversion (66% vs. 48% at 750 °C); selectivity towards olefins decreased only slightly over the redox catalyst due to non-selective combustion (CO_x selectivity below 3% across this temperature range). $Na_2WO_4/CaMnO_3$ achieved an olefin yield of 67% at T = 775 °C with 2.3% CO_x yield. Moreover, at the conditions shown, 88% or more of the H_2 produced was combusted, which can provide heat to the overall reaction and may contribute to the increase in *n*-hexane conversion.

3.3. Effect of temperature on product yields

A series of tests were conducted to assess the applicability of the four redox catalysts to *n*-hexane ROC and to study the resulting product distributions. Conversion of *n*-hexane proceeds largely via thermal cracking at the conditions tested (725 °C–775 °C), and olefin yields (*i.e.* ethylene, propylene, and C_{4+}) are therefore strongly dependent on temperature. Fig. 5 illustrates the relationships between *n*-hexane conversion, olefin selectivity, and temperature for each of the redox catalysts, at a fixed GHSV = 9000 h^{-1}. Olefin yields are differentiated by constant-yield contours.

$SrMnO_3$ showed the highest *n*-hexane conversion among the four redox catalysts, even at relatively low temperatures (82% at T = 725 °C), along with the highest CO_x selectivity (43%), indicating that its lattice oxygen participates significantly in non-selective combustion. $SrMnO_3$ was the only redox catalyst in this study to exhibit coke formation (Tables S3, S5; coke determination methods are described in Figure S1). Unpromoted $CaMnO_3$ converted less *n*-hexane but was more inherently selective to olefins, though olefin selectivity decreased significantly with increasing temperature. The activity towards *n*-hexane conversion and the significant CO_x selectivity of the base $SrMnO_3$ and $CaMnO_3$ redox catalysts is not entirely surprising, given that perovskite oxide-based catalysts have been explored for catalytic combustion or degradation of various hydrocarbons [25,26]. Promotion by 20 wt.% Na_2WO_4 consistently improves selectivity to olefins for both $SrMnO_3$ and $CaMnO_3$. CO_x yield from $CaMnO_3$ dropped by over 96% upon Na_2WO_4 promotion and olefin yield increased by 19% at 725 °C, indicating that Na_2WO_4 suppressed the non-selective combustion of *n*-hexane and olefins by $CaMnO_3$ and facilitated olefin yields in excess of the thermal cracking yields, as shown in Fig. 4. Similarly, $Na_2WO_4/SrMnO_3$ exhibited a 130–140% increase in olefin selectivity compared to $SrMnO_3$ at all temperatures tested. Complete reaction testing results can be found in Table S3.

Table 1
Product distribution of the *n*-hexane oxy-cracking reaction over the 20 wt.% $Na_2WO_4/CaMnO_3$ redox catalyst at GHSV = 9000 h^{-1} (m = 500 mg) and over a range of temperatures. Thermal background (*BG*) data at 725 °C and 775 °C are from an inert alumina-packed reactor.

	725 °C (*BG*)	725 °C	750 °C	775 °C	775 °C (*BG*)
Conversion (mol %)					
n-hexane	33.6	49.4	65.7	81.7	66.7
H_2 (to H_2O)	–	89.0	100.0	89.0	–
Selectivity (carbon mol %)					
CH_4	9.7	9.1	10.0	10.5	10.4
C_2H_4	36.9	36.8	40.3	43.2	42.8
C_3H_6	25.9	25.0	24.0	21.9	24.1
butenes	15.9	14.9	12.2	9.5	11.0
1,3-butadiene	1.9	3.2	4.6	6.2	4.2
C_2–C_4 paraffins	4.2	4.3	4.0	3.7	4.1
C_{5+} (paraffins, olefins)	4.8	4.6	3.1	1.6	2.3
CO	–	0.0	0.0	0.0	–
CO_2	–	1.1	1.6	2.8	–

To further understand the effect of temperature on the oxy-cracking reaction, we examined the products formed over the Na_2WO_4-promoted $CaMnO_3$, focusing on two aspects: (1) the combustion (via the redox catalyst) of any resulting hydrogen, to form H_2O, and; (2) the formation of light olefins compared to that of CO_x compounds. On the first point, the ability to perform selective hydrogen combustion (SHC) is a key functionality for metal oxides employed in ROC; moreover, SHC has a complex dependence on reaction temperature. Selective combustion of H_2 to H_2O shifts the dehydrogenation equilibrium towards the olefin product and provides internal heat to the reactor, closing the heat balance and enabling auto-thermal cracking operation. On the other hand, the formation of easily condensable water facilitates separation with reduced energy consumption. These benefits lie in contrast to non-selective combustion, which would lead to CO_x formation and decrease the yield of olefin products.

Table 1 summarizes the performance of the $Na_2WO_4/CaMnO_3$ redox catalyst in terms of key characteristics from the *n*-hexane oxy-cracking reaction at temperatures from 725 °C to 775 °C. Thermal background data are also given for T = 725 °C and 775 °C. At all three temperatures, in the presence of the redox catalyst, > 88% of the H_2 co-produced in cracking reactions was combusted. Despite the significant combustion capability of $Na_2WO_4/CaMnO_3$, there is relatively little generation of CO_x compounds at any of the temperatures studied, indicating that this redox catalyst is capable of performing SHC under *n*-hexane oxy-cracking conditions. CO_2 selectivity reached a maximum of 2.8% at 775 °C compared to a total olefin selectivity of 82.4%, and CO was never detected. While the olefin selectivity remained generally constant (from 85.5% at 725 °C to 82.4% at 775 °C), the selectivity towards longer chain olefins decreased with increasing temperature due to the higher cracking severity. Ethylene was the favored product at each temperature, most significantly at 775 °C, while propylene and the C_4 olefins (*e.g.* 1-butene, 1,3-butadiene) had greater selectivity at the low-temperature end of the range (25.0% and 18.1%, respectively). Neither coke nor aromatic compounds were detected in these experiments (verified via MS on-stream analysis, Figure S1).

3.4. Redox catalyst characterization and mechanistic investigation

Redox catalysts are unique in that both the surface and bulk properties can affect reaction performance—the surface facilitates both desired and undesired chemical reactions, whereas the bulk supplies active lattice oxygen as the oxidant. In this section, we endeavor to explain the performance of Na_2WO_4-promoted $SrMnO_3$ and $CaMnO_3$ via characterization of as-prepared and cycled variants of these redox catalysts as well as the unpromoted perovskite oxides. The results shown in Figs. 3 and 5 indicate that perovskite oxide promotion by

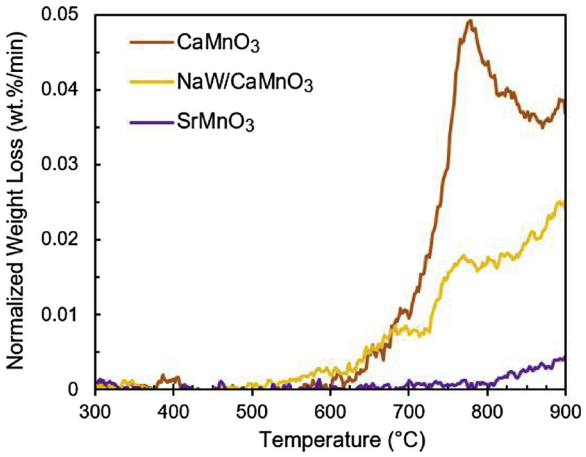

Fig. 6. O_2-TPD results of three redox catalysts. Samples were held under 10% atmosphere of the adsorbing gas for 30 min at 900 °C, ramped down to 150 °C at 10 °C/min, and purged under an inert He environment for 60 min prior to testing. TG weight loss rates were normalized by initial sample mass. Conditions: m = 30–50 mg, F = 180 mL/min He, ramping rate = 5 °C/min.

Na_2WO_4 alters the oxygen donation properties of $SrMnO_3$ and $CaMnO_3$ redox catalysts, leading to enhanced olefin yields. Generally, the increase in ethylene and propylene yields for the promoted samples was due to increased olefin selectivity rather than higher *n*-hexane conversion when compared to their unpromoted counterparts; in fact, conversion was suppressed by the presence of Na_2WO_4 for both redox catalyst systems whereas selectivity was significantly enhanced (Fig. 5). Therefore, it can be instructive to investigate the effect of Na_2WO_4 on the oxygen donation and surface properties of the redox catalysts. We begin by assessing the ability of the redox catalysts to release oxygen directly into the gas phase (oxygen uncoupling) via oxygen temperature-programmed desorption (O_2-TPD) experiments. It is worth noting that oxygen release determined via O_2-TPD is distinct from oxygen donation capacity under a reducing gas (*i.e.* as in Fig. 2), and the two cannot be directly correlated.

The effect of Na_2WO_4 promotion on oxygen release was characterized using O_2-TPD, with redox catalyst mass loss measured on a SETARAM TGA instrument (Fig. 6). O_2-TPD results for $SrMnO_3$ did not show significant desorption of oxygen species until a rise starting at 800 °C which was attributed to the release of lattice oxygen resulting from oxygen vacancy formation and reduction of Mn cations [27,28]. Conversely, significant O_2 loss from $CaMnO_3$ was detected beginning at 625 °C, in agreement with previous reports showing that $CaMnO_3$ will spontaneously release its lattice oxygen under inert atmospheres as low as 600 °C [27]. Desorbed surface or chemisorbed oxygen species, while potentially present, could not be differentiated from released lattice oxygen. Oxygen desorption and lattice oxygen release were suppressed by promotion with Na_2WO_4 as indicated by the O_2-TPD curve for $Na_2WO_4/CaMnO_3$ in Fig. 6; loss of oxygen from $CaMnO_3$ fell by 41% (from 1.9 to 1.1 wt.%) upon Na_2WO_4 promotion. $Na_2WO_4/SrMnO_3$ was not tested due to the lack of meaningful oxygen release by $SrMnO_3$

The O_2-TPD results could explain both the lowered *n*-hexane conversion of $Na_2WO_4/CaMnO_3$ compared to $CaMnO_3$ and (in part) the increased selectivity towards olefins (Fig. 5), as electrophilic oxygen species and more readily available oxygen evolved from the bulk would provide an abundance of non-selective oxidant for undesirable CO_x formation (as observed in the *n*-hexane TPR for $CaMnO_3$ in Fig. 3). Consistent with previous reports on ethane ODH with Ruddlesden-Popper-structured redox catalysts [23,24], the O_2-TPD and isothermal ROC reaction results indicate that inhibiting oxygen release properties from a mixed oxide can improve its selectivity towards olefins at the expense of lowered activity. However, such a principle cannot be used to compare different mixed oxides with varying compositions and

Table 2
Surface cation atomic percentages for six redox catalyst variants from XPS analysis. Carbon and oxygen are excluded. Surface enrichment and suppression of cations, shown in parentheses, are calculated using observed percentages from XPS in combination with expected percentages from overall stoichiometry.

Redox Catalyst	Sr 3*d* / Ca 2*p*	Mn 2*p*	Na 1*s*	W 4*f*
$SrMnO_3$ (*fresh*)	74.9% (1.5)	25.2% (0.5)	–	–
$Na_2WO_4/SrMnO_3$ (*fresh*)	52.9% (1.3)	16.1% (0.4)	14.2% (1.1)	16.7% (2.6)
$Na_2WO_4/SrMnO_3$ (*cycled*)	52.3% (1.3)	17.3% (0.4)	16.5% (1.3)	13.9% (2.1)
$CaMnO_3$ (*fresh*)	67.8% (1.4)	32.2% (0.6)	–	–
$Na_2WO_4/CaMnO_3$ (*fresh*)	41.9% (1.0)	19.1% (0.5)	22.2% (2.2)	16.7% (3.3)
$Na_2WO_4/CaMnO_3$ (*cycled*)	44.7% (1.1)	20.1% (0.5)	20.4% (2.0)	14.9% (2.9)

hence surface properties. For instance, unpromoted $SrMnO_3$, with inferior oxygen donation properties compared to unpromoted $CaMnO_3$, gave higher *n*-hexane conversion and lower olefin selectivity. This was likely a result of their distinct surface properties, as will now be discussed.

Near-surface atomic percentages found via X-ray photoelectron spectroscopy (XPS) for six $SrMnO_3$- and $CaMnO_3$-based redox catalysts exhibited a relative enrichment of Na and W atoms compared to Sr, Ca, and Mn (Table 2). In this context, enrichment (or suppression) was defined as the ratio of the observed near-surface metal content (in atomic percent) to the expected metal percentage based on the overall sample stoichiometry. W atoms were enriched in the near-surfaces of as-prepared $Na_2WO_4/CaMnO_3$ (W = 3.3) and $Na_2WO_4/SrMnO_3$ (W = 2.6), while Na enrichment was significant for the promoted $CaMnO_3$ (Na = 2.9) and more modest for the promoted $SrMnO_3$ (Na = 1.1). After 25 redox cycles, Na_2WO_4 remained prominent in the near-surface of each redox catalyst (Table 2), rather than moving into the bulk in response to repeated redox stresses or volatilizing due to high-temperature operation. As such, the XPS analysis for each sample indicates a significant Na_2WO_4 enrichment on the redox catalyst surface which is resistant to change after 25 redox cycles with *n*-hexane. Due to the escape depth of XPS measurements (~10 atomic layers), the degree of Na_2WO_4 enrichment on the immediate surface is likely to be much stronger than indicated, as suggested in studies on related systems [19,22]. Carbon and oxygen were not included in enrichment and suppression calculations; C 1*s* and O 1*s* XPS spectra for all samples are provided in Figures S2–S5.

The selectivity of perovskites for partial oxidation reactions such as methane to syngas and ethane oxidative dehydrogenation has previously been related to the relative amounts of lattice oxygen to surface oxygen species, often estimated from the XPS O 1*s* spectra [24,29,30]. While these species were clearly present in the asymmetric O 1*s* spectra of as-prepared $SrMnO_3$ and $CaMnO_3$ (with $SrMnO_3$ showing slightly higher surface oxygen species), the presence of WO_4^{2-} species obfuscated the relevant peaks in the Na_2WO_4-promoted samples (Figures S3–S4). Surface Mn was under-represented in both unpromoted samples, though Na_2WO_4 promotion further decreased the near-surface Mn cations in both cases (Table 2). Mn 2*p* spectra of the as-prepared and Na_2WO_4-promoted redox catalysts are presented in Figures S6–S7.

To understand the differences in olefin selectivity between as-prepared and Na_2WO_4-promoted redox catalysts, we examined the Sr 3*d* and Ca 2*p* XPS spectra of $SrMnO_3$ and $CaMnO_3$ for changes in (Sr,Ca) surface species upon promotion. The characteristic XPS peaks of these alkaline earth ions, particularly Sr, indicated a suppression of surface species upon promotion with Na_2WO_4. Fig. 7 shows the fitted XPS spectra for Sr 3*d* (Fig. 7a) and Ca 2*p* (Fig. 7b) on $SrMnO_3$-based and $CaMnO_3$-based redox catalysts, respectively. Details of the fit peaks are given in Tables S6–S7. All spectra were well fit by a pair of doublets, with one doublet consistent with bulk oxide species and another consistent with surface species [31]. Line shape fitting for the Sr 3*d* spectra of $SrMnO_3$ required two doublets: the Sr $3d_{5/2}$ peak at 132.3 eV binding energy (BE) was assigned to bulk Sr from the $SrMnO_3$ lattice, [32–35], while a second doublet with its characteristic Sr $3d_{5/2}$ peak at 132.8 eV was attributed to a combination of Sr bonded with surface oxygen species ($SrCO_3$, $Sr(OH)_2$) [31,36,37] and a near-surface SrO/Sr_2MnO_4 region (Sr/Mn = 3.0 for the $SrMnO_3$ near-surface) [38,39]. Each doublet exhibited an energy separation of 1.7 eV, consistent with previous literature [33,36,40]. Upon promotion of $SrMnO_3$ with 20 wt.% Na_2WO_4, the presence of free SrO, $Sr(OH)_2$, and $SrCO_3$ in the near-surface was diminished by over 90%, evident from the drastic reduction of the higher BE Sr 3*d* doublet for surface Sr and the drop in overall near-surface Sr enrichment (1.5 to 1.3), which corresponds to the 40% increase in olefin selectivity of the $Na_2WO_4/SrMnO_3$ redox catalyst. CO_2-TPD results confirmed an absence of strongly chemisorbed CO_2 species on $Na_2WO_4/SrMnO_3$, whereas CO_2 adsorbed on unpromoted $SrMnO_3$ was significantly more stable and amounted to nearly 1 wt.% of the sample after exposure (see Figure S5). The suppression of Sr surface species resulting from Na_2WO_4 surface enrichment, and the subsequent inhibition of hydrocarbon combustion activity, was critical to achieving the high olefin yields demonstrated in Fig. 5. This finding is consistent with previous literature identifying the important role of surface Sr^{2+} in catalytic combustion reactions over Sr-containing perovskite catalysts [25].

Surface oxides, hydroxides, and carbonates were significantly less prominent for the undoped $CaMnO_3$ system than for the $SrMnO_3$ (accounting for 12.2% of Ca ions vs. 32.9% of Sr ions), and therefore the suppression of such species by Na_2WO_4 was less significant, as depicted in Fig. 7b. The Ca 2*p* spectra exhibited a primary feature at around 345.3 eV consistent with the characteristic Ca $2p_{3/2}$ peak for lattice Ca from $CaMnO_3$ [32]. A high BE shoulder located at 346.7 eV indicated the presence of surface-type Ca, which can be assigned to CaO, $CaCO_3$, $Ca(OH)_2$, or a combination thereof [32,36,41], as would be expected from the surface enrichment of Ca from the $CaMnO_3$ lattice (1.4, Table 2). Upon promotion with 20 wt.% Na_2WO_4, surface-type Ca species decreased from 12.2% to 7.5% of all detected Ca which, combined with the near-surface depletion of Ca upon promotion with Na_2WO_4 (1.4 to 1.0), gave an overall decrease in Ca surface species of 62%. The suppression of surface species resulting from Na_2WO_4 enrichment may inhibit deep oxidation, resulting in greater olefin selectivity for the *n*-hexane oxy-cracking reaction in the presence of $Na_2WO_4/CaMnO_3$ as compared to $CaMnO_3$ (Fig. 5) [23,30].

After 25 redox cycles under *n*-hexane, the Ca 2*p* spectra of the $Na_2WO_4/CaMnO_3$ were unchanged. For cycled $Na_2WO_4/SrMnO_3$, the Sr 3*d* spectra reveal only a slight reemergence of surface-type Sr (11.2%), indicating that the cycled sample maintained a significant suppression of the surface Sr species from $SrMnO_3$ (32.9%). Additional spectra for the cycled samples are presented in Figures S8–S10. The presence of significantly more surface hydroxides and carbonates on as-prepared $SrMnO_3$ compared to $CaMnO_3$ can be attributable to both the stronger basicity of SrO, which strongly chemisorbs H_2O and CO_2 [36,42], and to an elevated presence of Sr in the near-surface due to its surface separation, as reported in multiple studies of Sr-containing perovskites [38–40,42]. (XRD patterns indicated that such phase separation did not affect the bulk, as will be discussed later.) For both $SrMnO_3$ and $CaMnO_3$, the suppression of surface-type Sr and Ca species upon Na_2WO_4 promotion was associated with a significant decline in CO_x selectivity at reaction conditions, as shown in Fig. 8.

Surface enrichment of Na_2WO_4 was shown to have a significant

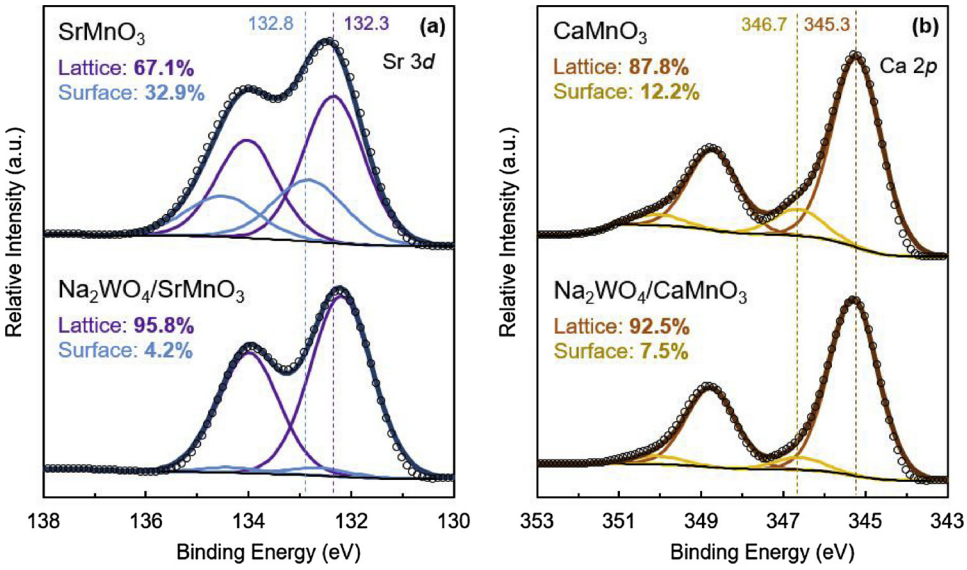

Fig. 7. Photoemission spectra of Sr 3*d* (a) and Ca 2*p* (b) for the $SrMnO_3$- and $CaMnO_3$-based redox catalysts, respectively, using an Al Kα X-ray source (1486.7 eV). Binding energies (BE) were referenced to the C 1*s* peak for adventitious carbon at 284.6 eV. Dotted lines indicate BE value for the characteristic peaks of lattice (low BE) and surface (high BE) doublets for the unpromoted $(Sr,Ca)MnO_3$.

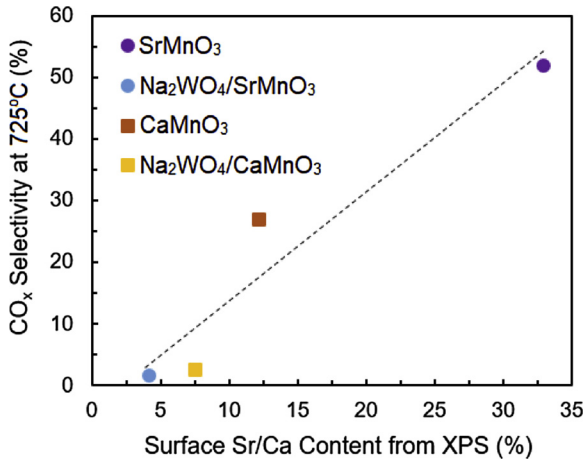

Fig. 8. Relationship between the accommodation of surface-type Sr/Ca species and CO_x selectivity at T = 725 °C and GHSV = 4500 h^{-1} (F_{Ar} = 75 mL/min, m = 500 mg). $y_{n\text{-hexane}} \approx 0.13$, step duration = 40 s. The dashed line is used to show the general trend and does not representative quantitative correlation.

suppression effect on surface cation and oxygen species, which resulted in greater olefin selectivity and improved yields from *n*-hexane ROC. The nature of this enrichment was further studied with low-energy ion scattering spectroscopy (LEIS), and we determined that Na_2WO_4 comprised the outermost surface layer of the $Na_2WO_4/CaMnO_3$ redox catalyst upon promotion. Fig. 9a shows LEIS spectra for the 20 wt.% $Na_2WO_4/CaMnO_3$ redox catalyst surface with increasing doses of sputter-etching using 0.5 keV Ar^+ sputtering source (1×10^{15} Ar^+ ions/cm^2 corresponding to the removal of approximately one atomic monolayer) and with a 3 keV He^+ probe beam [24]. Initial sputtering with 0.5×10^{15} cm^{-2} (green) revealed an outermost surface layer composed of O, Na, and W, with a slight shoulder in the vicinity of Ca and a less significant shoulder where a Mn peak would be expected, altogether indicating the predominance of Na_2WO_4 in the surface monolayer. Subsequent removal of the first few atomic monolayers revealed a Ca peak, but not a Mn peak; this may indicate that the $CaMnO_3$ substrate terminates in a CaO plane or Ca-rich phase (*e.g.* CaO, Ca_2MnO_4) or that Ca from the $CaMnO_3$ lattice migrates and reacts with Na_2WO_4 to form a calcium tungstate (*e.g.* $CaWO_4$) phase near the surface. A cumulative dosing of 20×10^{15} cm^{-2} was sufficient to reveal a Mn peak. Depth profiling of the main elements shown in Fig. 9b featured Na and W signals which rose more rapidly than those of Ca and

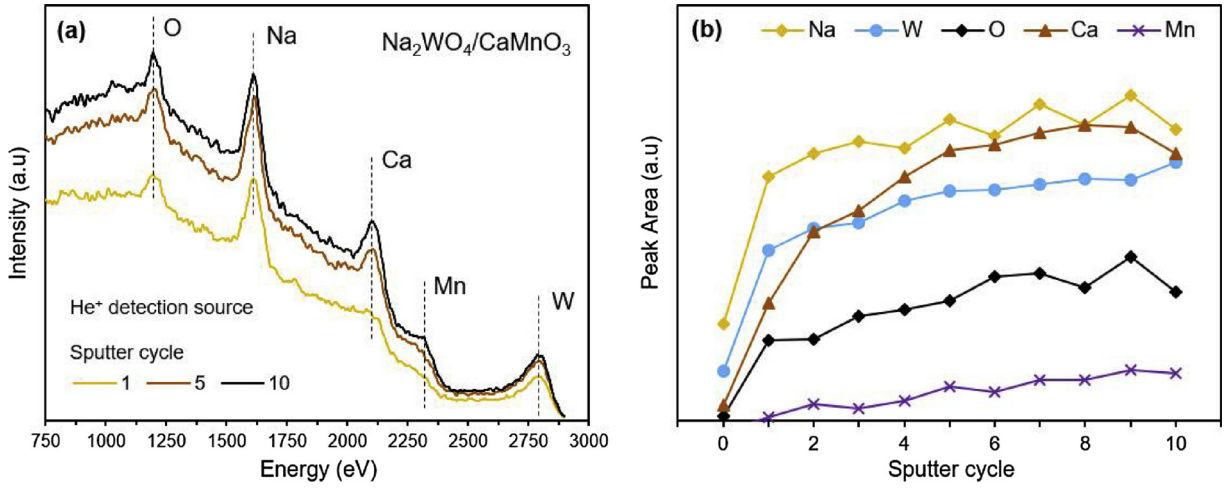

Fig. 9. LEIS spectra for 20 wt.% $Na_2WO_4/CaMnO_3$ acquired using a 3 keV He^+ probe beam. (a) Surface scans after varying amounts of 0.5 keV Ar^+ sputter-etching; one sputter cycle corresponds to 0.5×10^{15} Ar^+ ions cm^{-2}. (b) Depth profiles of Na, W, O, Ca, and Mn, showing peak areas as a function of sputter cycle, up to a maximum dose of 5.0×10^{15} cm^{-2}.

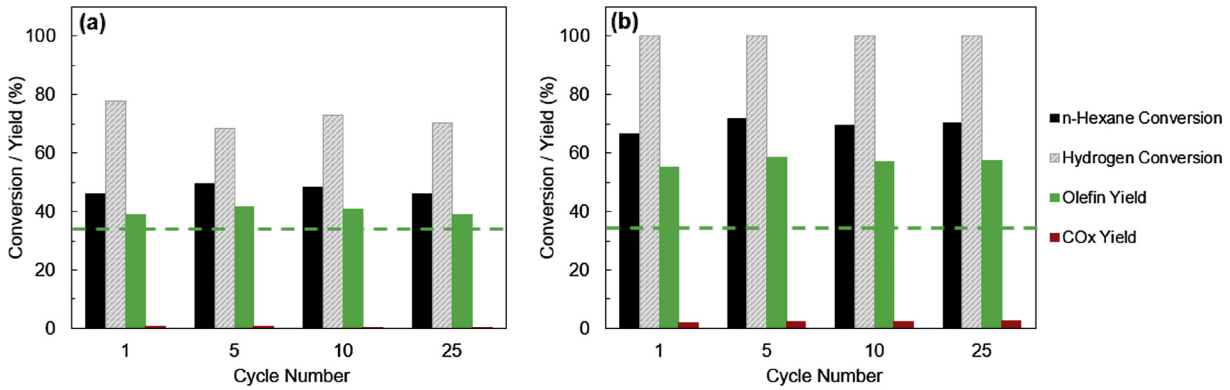

Fig. 10. A comparison of reaction characteristics over the course of 25 *n*-hexane oxy-cracking cycles for (a) $Na_2WO_4/SrMnO_3$ and (b) $Na_2WO_4/CaMnO_3$. Thermal background olefin yield is given as a dashed line. Conditions: T = 725 °C, GHSV = 4500 h^{-1} (F_{Ar} = 75 mL/min, m = 500 mg), $y_{n\text{-hexane}} \approx 0.13$, step duration = 40 s.

particularly Mn with increasing sputtering, also indicating that the Na_2WO_4 promoter was at a higher concentration than $CaMnO_3$ near the immediate surface. Taken together, the surface-sensitive characterization and reaction performance data of (Sr,Ca)MnO_3-based redox catalysts have revealed the crucial role of the Na_2WO_4 surface layer in achieving high olefin yields for *n*-hexane ROC.

3.5. Evaluation and literature comparison of redox catalyst performance and stability

Lastly, we demonstrate with XRD after 25 cycles of *n*-hexane ROC that the $Na_2WO_4/SrMnO_3$ and $Na_2WO_4/CaMnO_3$ redox catalysts are structurally stable and capable of maintaining desirable properties (*n*-hexane conversion, olefin selectivity, SHC). Fig. 10 gives key reaction characteristics for multiple *n*-hexane oxy-cracking cycles using $Na_2WO_4/SrMnO_3$ (Fig. 10a) and $Na_2WO_4/CaMnO_3$ (Fig. 10b) at T = 725 °C and GHSV = 4500 h^{-1}. Each sample was pre-treated under ethane at 750 °C. Both redox catalysts show stable conversion of *n*-hexane and of hydrogen as well as olefin yields that are consistently higher than the thermal background (given by the dashed line), with $Na_2WO_4/CaMnO_3$ showing the greater activity (and slightly lower selectivity).

$Na_2WO_4/SrMnO_3$ preserves its high selectivity towards hydrogen combustion over the 25 cycles, with the last cycle showing low CO_x formation (0.28% CO_x yield). The slight decline in CO_x generation over 25 cycles may be explained by a decrease in available oxygen, as evidenced by the XRD pattern for the cycled $Na_2WO_4/SrMnO_3$ redox catalyst (Fig. 11a). Non-selective combustion of *n*-hexane or olefins to CO_x may be exacerbated by a fully restored oxygen carrier and the presence of surface α-oxygen species. Nonetheless, the hydrogen conversion and SHC capability by this material is not negatively affected, and $Na_2WO_4/SrMnO_3$ remains an attractive material for the application.

$Na_2WO_4/CaMnO_3$ shows greater oxygen donation and higher conversions in general than the $SrMnO_3$-based material, leading to higher CO_x yields (1.7–2.8%); this redox catalyst is capable of combusting 100% of the generated H_2 in the system. This total combustion of H_2 may contribute to the elevated *n*-hexane conversion over this redox catalyst (69–71% for $Na_2WO_4/CaMnO_3$, compared to 48–50% for $Na_2WO_4/SrMnO_3$) and the higher olefin yields which result (55–58% vs. 39–41% at 725 °C). The results obtained for $Na_2WO_4/CaMnO_3$ compare favorably with the catalyst developed by Liu et al., which produced approximately 12–13% CO_x yield along with 50% olefin yield at 750 °C; for 20 wt.% $Na_2WO_4/CaMnO_3$ at 725 °C, a maximum of 58% olefin yield was achieved along with only 2.8% maximum CO_x yield while also decreasing the temperature requirement [10,11]. In another study by Boyadjian et al., Li/MgO catalysts achieved 17% light olefin yield from *n*-hexane at 575 °C while producing 7% CO_x yield [12]. The performance of $Na_2WO_4/CaMnO_3$ as compared to literature catalysts is best encapsulated in the ratio of carbon utilization for light olefin yield vs. CO_x yield, which was approximately 21:1 in this work, compared to 4.2:1 (Liu et al.) and 2.5:1 (Boyadjian et al.). $Na_2WO_4/CaMnO_3$ is thus a stable and very promising redox catalyst for *n*-hexane oxidative cracking when operated at or near 725 °C.

Fig. 11a–b shows results from XRD experiments on as-prepared and cycled samples based on $SrMnO_3$ and $CaMnO_3$, respectively. These patterns indicate that both $Na_2WO_4/SrMnO_3$ and $Na_2WO_4/CaMnO_3$ were resistant to promoter-oxide interactions during cycling at T = 725 °C. Multiple phases were observed in the $SrMnO_3$ system: a minor Sr_2MnO_4 impurity was present which was later undetectable after promotion with Na_2WO_4, and the brownmillerite phase $Sr_2Mn_2O_5$ was present in nearly equal proportion to $SrMnO_3$ for the cycled $Na_2WO_4/SrMnO_3$ sample. The latter phase indicated an incomplete regeneration of the perovskite structure. Lower operating temperatures therefore have the effect of lowering the oxygen capacity of the redox catalyst by limiting phase regeneration, but increasing selectivity towards hydrogen combustion, as supported by the results of Fig. 10. The presence of $Sr_2Mn_2O_5$ also suggests that complete regeneration of the perovskite phase is a slower process for the hexagonal $SrMnO_3$ than for the cubic $CaMnO_3$.

4. Conclusion

In this work, we demonstrated the effectiveness of several redox catalysts for the redox oxidative cracking (ROC) of naphtha using *n*-hexane as a model compound. At 725 °C and 4500 h^{-1}, Na_2WO_4-promoted $CaMnO_3$ achieved over 72% increase in olefin yields, on a relative basis, over thermal cracking while completely combusting H_2. The redox catalyst exhibited < 3% CO_x yield and maintained excellent stability over 25 redox cycles. Na_2WO_4-promoted $SrMnO_3$ also demonstrated superior olefin yield compared to thermal cracking with COx formation as low as 0.28%. The greater olefin yields and low CO_x selectivity were attributed primarily to the selective combustion of H_2 by Na_2WO_4/(Sr,Ca)MnO_3. Promotion by 20 wt.% Na_2WO_4 was highly effective to improve the selectivity of the redox catalysts, which was attributed to a surface enrichment of Na and W and significant alteration of the surface sites of $SrMnO_3$ and $CaMnO_3$.

XRD analysis confirmed the phase stability, and promoter-oxide interactions were not observed after cycling. Surface-sensitive LEIS and XPS characterization revealed an outermost surface layer of was covered by Na_2WO_4, and near-surface regions for Na_2WO_4/(Sr,Ca)MnO_3 were significantly enriched in Na and W but deficient in Mn. Sr 3*d* spectra from XPS showed a 90% decrease in SrO/$Sr(OH)_2$/$SrCO_3$ surface species from $SrMnO_3$ upon promotion with Na_2WO_4, while similar Ca-containing surface species on $CaMnO_3$ were diminished by 62% with promotion. Correspondingly, we observed 97% suppression in CO_x selectivity with Na_2WO_4-promoted $SrMnO_3$ and 90% suppression for

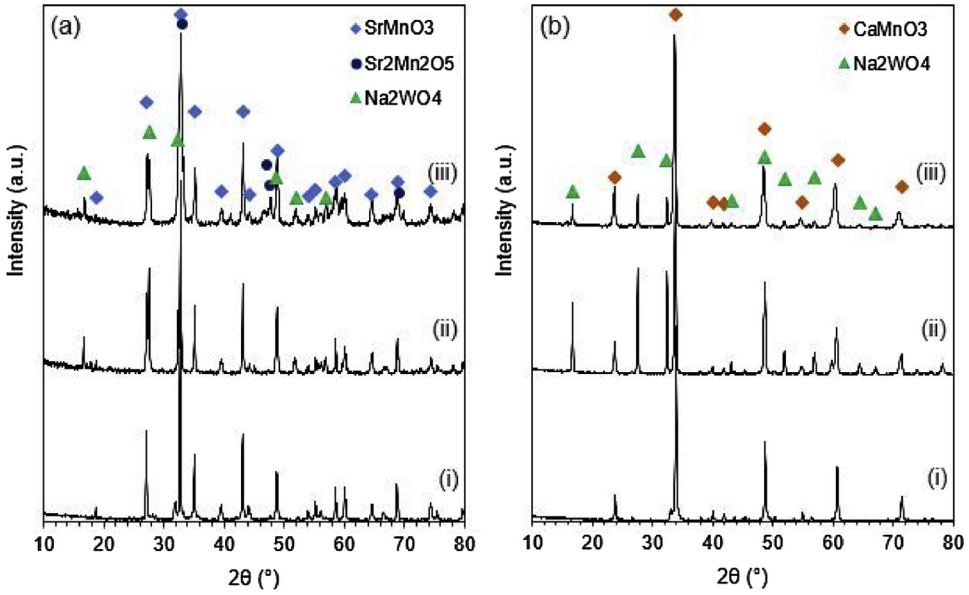

Fig. 11. XRD patterns for all redox catalysts. (a) Patterns for (i) $SrMnO_3$, (ii) $Na_2WO_4/SrMnO_3$, (iii) cycled $Na_2WO_4/SrMnO_3$. (b) Patterns for (i) $CaMnO_3$, (ii) $Na_2WO_4/CaMnO_3$, (iii) cycled $Na_2WO_4/CaMnO_3$. Cycled samples tested and re-oxidized at T = 725 °C, GHSV = 4500 h^{-1} for 25 cycles.

$Na_2WO_4/CaMnO_3$. Na_2WO_4 promotion also inhibited lattice oxygen release from $CaMnO_3$. Such effects, resulting from the surface enrichment of Na_2WO_4, suppressed non-selective combustion reactions and significantly enhanced olefin yields. Through the combination of reaction and characterization, the role of Na_2WO_4 was determined, and Na_2WO_4-promoted perovskite oxides are identified as promising redox catalysts for the oxidative cracking of *n*-hexane.

Acknowledgments

This work was supported by the U.S. National Science Foundation (Award No. CBET-1604605) and the Kenan Institute for Engineering, Technology and Science at NC State University. The authors acknowledge the use of the Analytical Instrumentation Facility (AIF) at North Carolina State University, which is supported by the State of North Carolina and the National Science Foundation. The authors also acknowledge the assistance from Dr. Kun Zhao at Guangzhou Institute of Energy Conversion, Chinese Academy of Sciences, for help in XPS measurements, and Dr. Henry Luftman at the Surface Characterization Facility of Lehigh University, for help in LEIS measurements.

Appendix A. Supplementary data

Supplementary material related to this article can be found, in the online version, at doi:https://doi.org/10.1016/j.apcatb.2019.01.048.

Details on experimental oxygen donation calculations, details on oxygen utilization in the ROC process scheme, BET surface areas, expanded reaction data for redox catalysts and relevant thermal background at 4500 h^{-1} and 9000 h^{-1}, reaction data of redox catalysts at different particle size ranges and Na_2WO_4 wt.% loadings, additional details on determination of coke deposition, XPS C 1*s*, O 1*s*, Mn 2*p*, Ca 2*p*, and Sr 3*d* narrow scans for as-prepared, promoted, and cycled redox catalysts, additional details on XPS spectra deconvolution and peak fitting, and CO_2-TPD results on $SrMnO_3$-based redox catalysts.

References

[1] H. Zimmermann, R. Walzl, Ethylene, Ullmann's Encycl. Ind. Chem, (2012), pp. 547–572, https://doi.org/10.1002/14356007.a10.
[2] J.V. Moreira, Steam Cracking: Kinetics and Feed Characterisation, (2015) https://fenix.tecnico.ulisboa.pt/downloadFile/1126295043834327/JVM_ExtendedAbstract.pdf.
[3] T. Ren, M. Patel, K. Blok, Olefins from conventional and heavy feedstocks: energy use in steam cracking and alternative processes, Energy 31 (2006) 425–451, https://doi.org/10.1016/j.energy.2005.04.001.
[4] International Energy Agency, Technology Roadmap: Energy and GHG Reductions in the Chemical Industry Via Catalytic Processes, (2013).
[5] R.C. Valencia, The Future of the Chemical Industry by 2050, (2013), https://doi.org/10.1002/3527602089.
[6] S.M. Sadrameli, Thermal/catalytic cracking of liquid hydrocarbons for the production of olefins: a state-of-the-art review I: thermal cracking review, Fuel 140 (2015) 102–115, https://doi.org/10.1016/j.fuel.2016.01.047.
[7] V.P. Haribal, Y. Chen, L. Neal, F. Li, Intensification of ethylene production from naphtha via a redox oxy- cracking scheme: process simulations and analysis, Engineering 4 (2018), https://doi.org/10.1016/j.eng.2018.08.001.
[8] S.M. Sadrameli, Thermal/catalytic cracking of liquid hydrocarbons for the production of olefins: a state-of-the-art review II: catalytic cracking review, Fuel 173 (2016) 285–297, https://doi.org/10.1016/j.fuel.2016.01.047.
[9] N. Rahimi, R. Karimzadeh, Catalytic cracking of hydrocarbons over modified ZSM-5 zeolites to produce light olefins: a review, Appl. Catal. A Gen. 398 (2011) 1–17, https://doi.org/10.1016/j.apcata.2011.03.009.
[10] X. Liu, W. Li, H. Zhu, Q. Ge, Y. Chen, H. Xu, Light alkenes preparation by the gas phase oxidative cracking or catalytic oxidative cracking of high hydrocarbons, Catal. Lett. 94 (2004) 31–36, https://doi.org/10.1023/B:CATL.0000019327.86674.98.
[11] X. Liu, W. Li, H. Xu, Y. Chen, Production of light alkenes with low CO2emission from gas phase oxidative cracking (GOC) of hexane, React. Kinet. Catal. Lett. 81 (2004) 203–209, https://doi.org/10.1023/B:REAC.0000019424.06619.28.
[12] C. Boyadjian, L. Lefferts, K. Seshan, Catalytic oxidative cracking of hexane as a route to olefins, Appl. Catal. A Gen. 372 (2010) 167–174, https://doi.org/10.1016/j.apcata.2009.10.030.
[13] C. Boyadjian, K. Seshan, L. Lefferts, A.G.J. van der Ham, H. van den Berg, Production of C3/C4 olefins from n-Hexane: conceptual design of a catalytic oxidative cracking process and comparison to steam cracking, Ind. Eng. Chem. Res. 50 (2011) 342–351.
[14] J. Adanez, A. Abad, F. Garcia-Labiano, P. Gayan, L.F. De Diego, Progress in chemical-looping combustion and reforming technologies, Prog. Energy Combust. Sci. 38 (2012) 215–282, https://doi.org/10.1016/j.pecs.2011.09.001.
[15] N. Ballarini, F. Cavani, A. Cericola, C. Cortelli, M. Ferrari, F. Trifirò, G. Capannelli, A. Comite, R. Catani, U. Cornaro, Supported vanadium oxide-based catalysts for the oxidehydrogenation of propane under cyclic conditions, Catal. Today 91–92 (2004) 99–104, https://doi.org/10.1016/j.cattod.2004.03.016.
[16] A.H. Elbadawi, M.Y. Khan, M.R. Quddus, S.A. Razzak, M.M. Hossain, Kinetics of Oxidative Cracking of n-Hexane to Olefins Over VOx/Ce-Al2O3 Under Gas Phase Oxygen-Free Environment, AIChE J. 63 (2017) 130–138, https://doi.org/10.1002/aic.
[17] F. Li, L.M. Neal, J. Zhang, Redox Catalysts for the Oxidative Cracking of Hydrocarbons, Methods of Making, and Methods of Use Thereof, WO 2018/049389 A1 (2018).
[18] L.M. Neal, S. Yusuf, J.A. Sofranko, F. Li, Oxidative dehydrogenation of ethane: a chemical looping approach, Energy Technol. 4 (2016) 1200–1208, https://doi.org/10.1002/ente.201600074.
[19] S. Yusuf, L.M. Neal, F. Li, Effect of promoters on manganese-containing mixed metal oxides for oxidative dehydrogenation of ethane via a cyclic redox scheme, ACS Catal. 7 (2017) 5163–5173, https://doi.org/10.1021/acscatal.7b02004.

[20] V.P. Haribal, L.M. Neal, F. Li, Oxidative dehydrogenation of ethane under a cyclic redox scheme: process simulation and analysis, Energy 119 (2017) 1024–1035, https://doi.org/10.1016/j.energy.2016.11.039.
[21] R.B. Dudek, Y. Gao, J. Zhang, F. Li, Manganese-containing redox catalysts for selective hydrogen combustion under a cyclic redox scheme, AIChE J. 00 (2018) 1–10, https://doi.org/10.1002/aic.16173.
[22] S. Yusuf, L. Neal, V. Haribal, M. Baldwin, H.H. Lamb, F. Li, Manganese silicate based redox catalysts for greener ethylene production via chemical looping – oxidative dehydrogenation of ethane, Appl. Catal. B Environ. 232 (2018) 77–85, https://doi.org/10.1016/j.apcatb.2018.03.037.
[23] Y. Gao, L.M. Neal, F. Li, Li-promoted LaxSr2-xFeO4-d core-shell redox catalysts for oxidative dehydrogenation of ethane under a cyclic redox scheme, ACS Catal. 6 (2016) 7293–7302, https://doi.org/10.1021/acscatal.6b01399.
[24] Y. Gao, F. Haeri, F. He, F. Li, Alkali Metal-Promoted La $_x$ Sr $_{2-x}$ FeO $_{4-\delta}$ Redox Catalysts for Chemical Looping Oxidative Dehydrogenation of Ethane, ACS Catal. (2018) 1757–1766, https://doi.org/10.1021/acscatal.7b03928.
[25] F. Polo-Garzon, V. Fung, X. Liu, Z.D. Hood, E.E. Bickel, Understanding the impact of surface reconstruction of perovskite catalysts on CH4 activation and combustion, ACS Catal. 8 (2018) 10306–10315, https://doi.org/10.1021/acscatal.8b02307.
[26] J. Chen, Z. He, G. Li, T. An, H. Shi, Y. Li, Visible-light-enhanced photothermocatalytic activity of ABO3-type perovskites for the decontamination of gaseous styrene, Appl. Catal. B, Environ. 209 (2017) 146–154, https://doi.org/10.1016/j.apcatb.2017.02.066.
[27] N. Galinsky, A. Mishra, J. Zhang, F. Li, Ca1 − xAxMnO3(A = Sr and Ba) perovskite based oxygen carriers for chemical looping with oxygen uncoupling (CLOU), Appl. Energy 157 (2015) 358–367, https://doi.org/10.1016/j.apenergy.2015.04.020.
[28] J. Vieten, B. Bulfin, F. Call, M. Lange, M. Schmücker, A. Francke, M. Roeb, C. Sattler, Perovskite oxides for application in thermochemical air separation and oxygen storage, J. Mater. Chem. A 4 (2016) 13652–13659, https://doi.org/10.1039/c6ta04867f.
[29] L.M. Neal, A. Shafiefarhood, F. Li, Dynamic methane partial oxidation using a Fe2O3@La0.8Sr0.2FeO3-d core-shell redox catalyst in the absence of gaseous oxygen, ACS Catal. 4 (2014) 3560–3569.
[30] N.A. Merino, B.P. Barbero, P. Eloy, L.E. Cadús, La1-xCaxCoO3perovskite-type oxides: identification of the surface oxygen species by XPS, Appl. Surf. Sci. 253 (2006) 1489–1493, https://doi.org/10.1016/j.apsusc.2006.02.035.
[31] E.J. Crumlin, E. Mutoro, Z. Liu, M.E. Grass, M.D. Biegalski, Y.L. Lee, D. Morgan, H.M. Christen, H. Bluhm, Y. Shao-Horn, Surface strontium enrichment on highly active perovskites for oxygen electrocatalysis in solid oxide fuel cells, Energy Environ. Sci. 5 (2012) 6081–6088, https://doi.org/10.1039/c2ee03397f.
[32] V. Celorrio, L. Calvillo, G. Granozzi, A.E. Russell, D.J. Fermin, AMnO3(A = Sr, La, Ca, Y) perovskite oxides as oxygen reduction electrocatalysts, Top. Catal. 61 (2018) 154–161, https://doi.org/10.1007/s11244-018-0886-5.
[33] S. Mno, E.Z. Kurmaev, M.A. Korotin, V.R. Galakhov, L.D. Finkelstein, E.I. Zabolotzky, N.N. Efremova, J. Mitchell, E.Z. Kurmaev, M.A. Korotin, V.R. Galakhov, L.D. Finkelstein, E.I. Zabolotzky, N.N. Efremova, Phys. Rev. B 59 (1999) 799–806.
[34] T. Saitoh, T. Mizokawa, A. Fujimori, M. Abbate, Electronic structure and magnetic states i studied by photoemission and x-ray-absorption spectroscopy, Phys. Rev. B Condens. Matter Mater. Phys. 56 (1997) 1290–1295, https://doi.org/10.1103/PhysRevB.56.1290.
[35] D.G. Popescu, N. Barrett, C. Chirila, I. Pasuk, M.A. Husanu, Influence of hole depletion and depolarizing field on the BaTiO3/La0.6Sr0.4MnO3 interface electronic structure revealed by photoelectron spectroscopy and first-principles calculations, Phys. Rev. B Condens. Matter Mater. Phys. 92 (2015) 1–11, https://doi.org/10.1103/PhysRevB.92.235442.
[36] J. Dupin, D. Gonbeau, P. Vinatier, A. Levasseur, Systematic XPS Studies of Metal Oxides, Hydroxides and Peroxides Systematic XPS studies of metal oxides, hydroxides and peroxides, Phys. Chem. Chem. Phys. 2 (2000) 1319–1324, https://doi.org/10.1039/a908800h.
[37] R.P. Vasquez, X-ray photoelectron spectroscopy study of Sr and Ba compounds, J. Electron Spectros. Relat. Phenomena. 56 (1991) 217–240, https://doi.org/10.1016/0368-2048(91)85005-E.
[38] H. Dulli, P.A. Dowben, S.H. Liou, E.W. Plummer, Surface segregation and restructuring of colossal-magnetoresistant manganese perovskites La0.65Sr0.35MnO3, Phys. Rev. B Condens. Matter Mater. Phys. 62 (2000) R14629–R14632, https://doi.org/10.1103/PhysRevB.62.R14629.
[39] W. Lee, J.W. Han, Y. Chen, Z. Cai, B. Yildiz, Cation size mismatch and charge interactions drive dopant segregation at the surfaces of manganite perovskites, J. Am. Chem. Soc. 135 (2013) 7909–7925, https://doi.org/10.1021/ja3125349.
[40] P. Decorse, E. Quenneville, S. Poulin, M. Meunier, A. Yelon, F. Morin, Chemical and structural characterization of La0.5Sr0.5MnO3 thin films prepared by pulsed-laser deposition, J. Vac. Sci. Technol. A Vacuum Surf. Film 19 (2001) 910–915, https://doi.org/10.1116/1.1368200.
[41] V. Celorrio, L. Calvillo, E. Dann, G. Granozzi, A. Aguadero, D. Kramer, A.E. Russell, D.J. Fermín, Oxygen reduction reaction at LaxCa1-xMnO3nanostructures: Interplay between A-site segregation and B-site valency, Catal. Sci. Technol. 6 (2016) 7231–7238, https://doi.org/10.1039/c6cy01105e.
[42] V. Young, T. Otagawa, XPS studies on strontium compounds, Appl. Surf. Sci. 20 (1985) 228–248, https://doi.org/10.1016/0378-5963(85)90083-2.